SUPPLEMENTARY INFORMATION

Low-temperature wafer-scale graphitization of silicon-carbide substrates towards reusable ultra-wide bandgap substrates

Se H. Kim, Hanjoo Lee, Dong Gwan Kim, Donghan Kim, Seugki Kim, Hyunho Yang, Yunsu Jang, Jangho Yoon, Hyunsoo Kim, Seoyong Ha, ByoungTak Lee, Jung-Hee Lee, Roy Byung Kyu Chung, Hongsik Park, Sungkyu Kim, Tae Hoon Lee, Hyun S. Kum

Supplementary Note 1 | DFT Simulation modeling workflow

The slab models had dangling bonds on the vacuum surface, which were terminated with pseudo-hydrogen atoms with appropriate fractional charges to prevent the generation of surface states. To determine the vacuum level, dipole corrections were introduced to compensate for the artificial dipole moment at the open ends (20 Å vacuum space along the c-axis) arising from the periodical boundary condition imposed in these calculations.

To search for an ideal hetero-interface, combinations of substrate and film Miller indices were scanned[1]. From these scans, optimized domain-matched configurations with the lowest mismatch strain, supercell area, and lattice vector length were identified. This process resulted in the discovery of domain-matched heterostructures between SiC and graphene surfaces, with a lattice mismatch of less than 4%, as shown in Supplementary Fig. 3c. A similar matching procedure was applied to generate the interface between the SiC/graphene and metal layers.

To replicate the graphene-formaton phenomenon during the MAG (Metal-Assisted Graphitization) process, AIMD simulations were performed in three main steps: (i) a Si-containing metal layer was generated by substituting (at. 20%) Si atoms for Ni; (ii) the SiC/Graphene/Si-dissolved metal heterostructure was relaxed through energy minimization to stabilize the initial atomic configuration of each model; and (iii) random displacements were introduced to the carbon atoms in the graphene layer to study the stabilization effect of metal catalysts from the interface interaction beetween the metal and graphene layers[2–4].

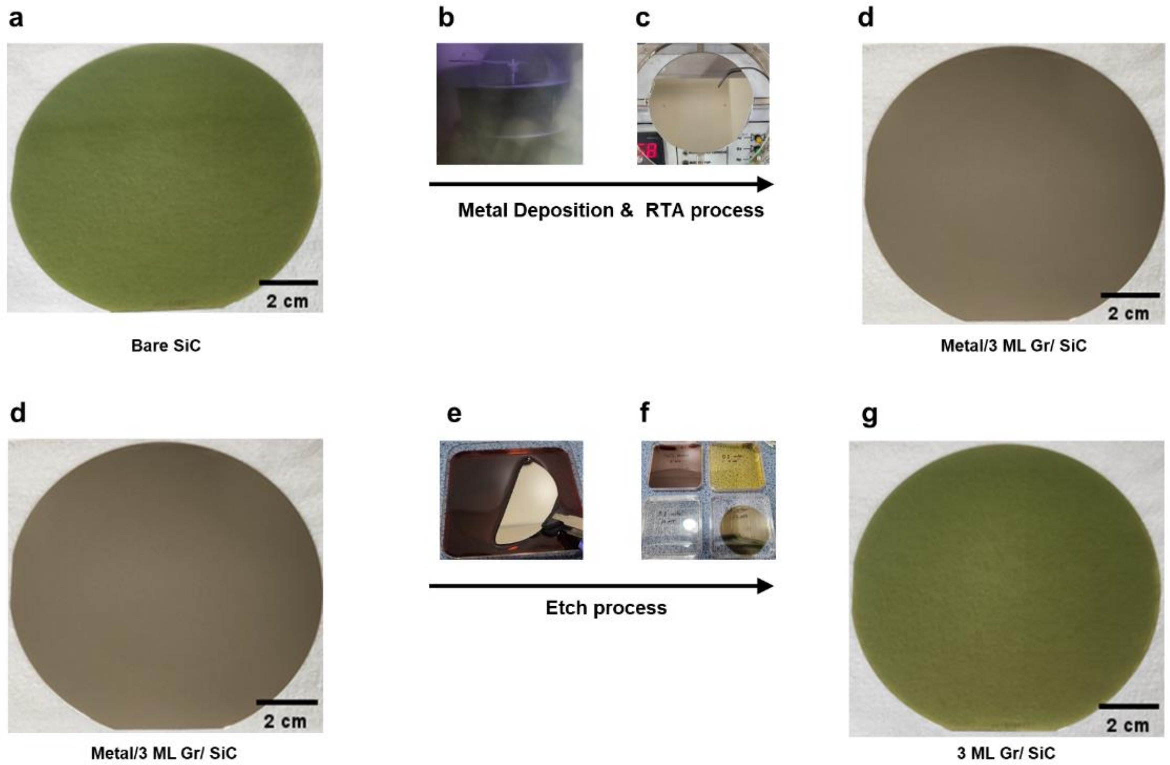

Supplementary Fig. 1 | Detailed MAG process. a, The SiC wafer is cleaned sequentially in acetone (5 minutes), and isopropyl alcohol (IPA) for 5 minutes each using an ultrasound bath and then dried with a nitrogen gun. **b,** Ni is deposited onto the SiC by sputtering at a pressure of 5×10^{-4} Torr in an Ar ambient (50 sccm) for 20 minutes. **c,** The sample is annealed in a rapid thermal annealing (RTA) chamber under specific conditions: a heating speed of 12°C/s, annealing for 3 minutes, and cooling by turning off the power. **d,** Graphene forms at the Ni/SiC interface through the MAG process. **e,** Ni is etched away using ferric chloride ($FeCl_3$) to expose the interface graphene. **f,** Once all visible traces of Ni are removed, the sample is gently agitated in fresh $FeCl_3$, followed by rinsing in deionized water. The surface is kept wet to prevent redeposition of Ni residues. **g,** The final result of the MAG process demonstrates graphene formation on the entire 4-inch SiC substrate.

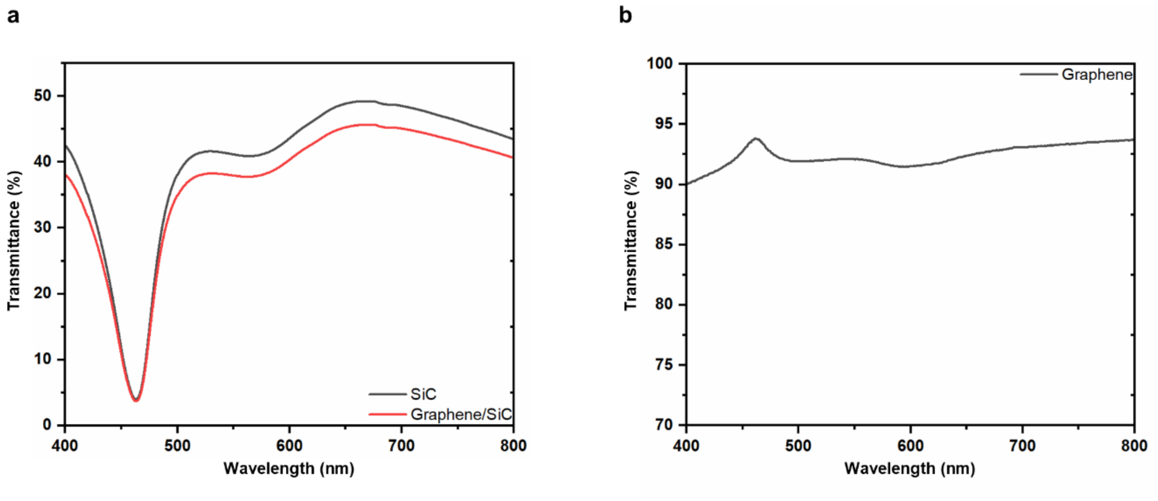

Supplementary Fig. 2 | UV-vis transmittance spectra in the wavelength range of 400 nm - 800 nm. a, UV-vis transmittance spectra of a SiC without graphene (red) and with graphene (black), showing reduced transmittance due to the graphene layer. **b,** The transmittance of graphene in the visible light is measured at 92.1% at 550 nm, indicating the presence of approximately 3.4 graphene monolayers on the SiC.

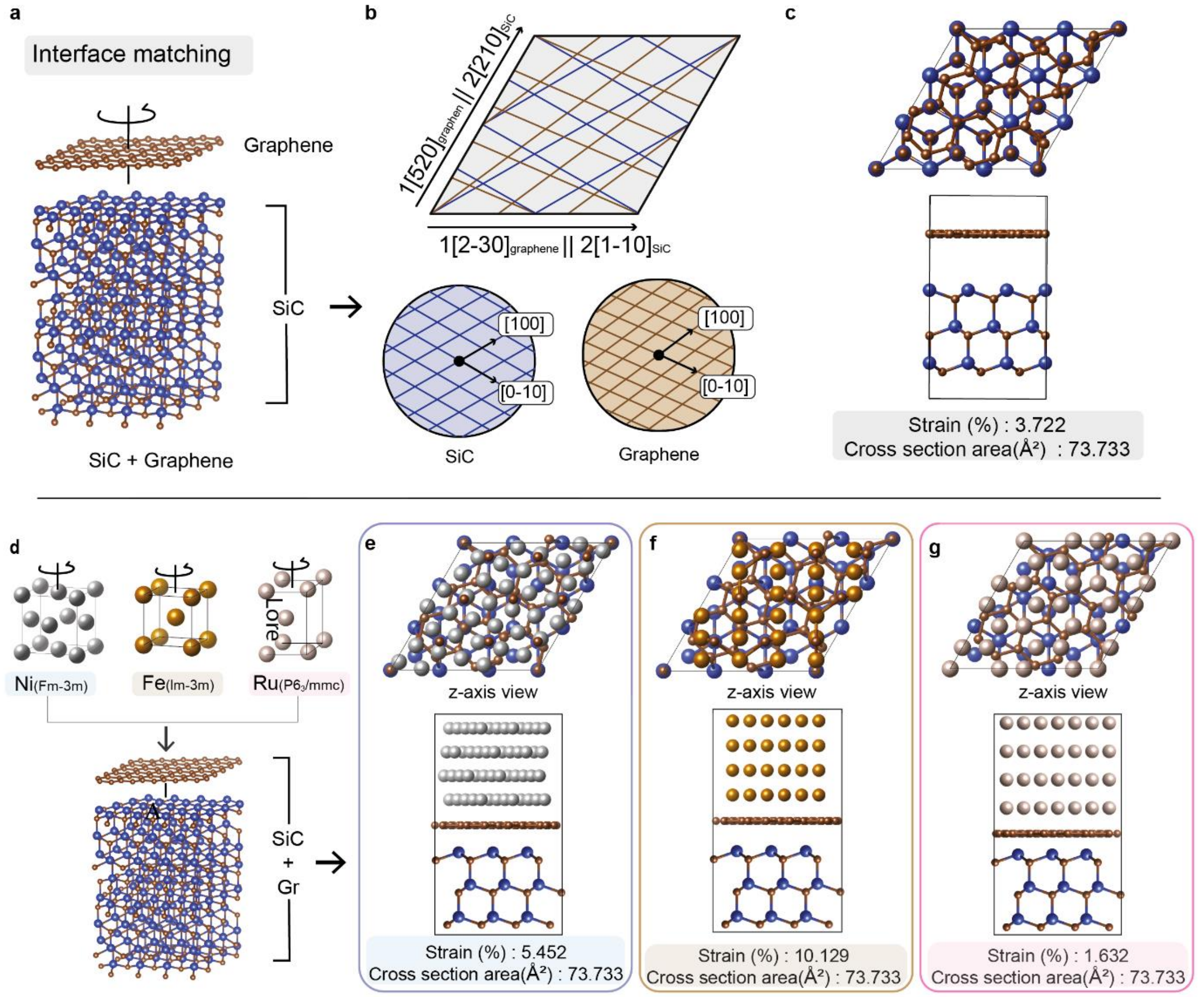

Supplementary Fig. 3 | Interface matching for modeling the SiC/graphene/metal structures. a, Interface construction for the SiC/Graphene structure. **b,** Domain-matched supercell construction for the SiC (blue) and graphene (brown) layers with corresponding lattice unit vectors. **c,** Top and side views of the optimized interface configuration (Si atoms are colored in blue, and C atoms are dark brown). **d,** Schematic illustration of the interface-matching process for the SiC/Graphene/Metal system, along with the crystal structures of Ni (Fm-3m), Fe (Im-3m), and Ru ($P6_3$/mmc) used for interface matching. **e-g,** Matched heterostructures used for the AIMD simulations: Ni (5.452% strain), Fe (10.129% strain), and Ru (1.632% strain), each with a cross-sectional area of 43.256 Å^2.

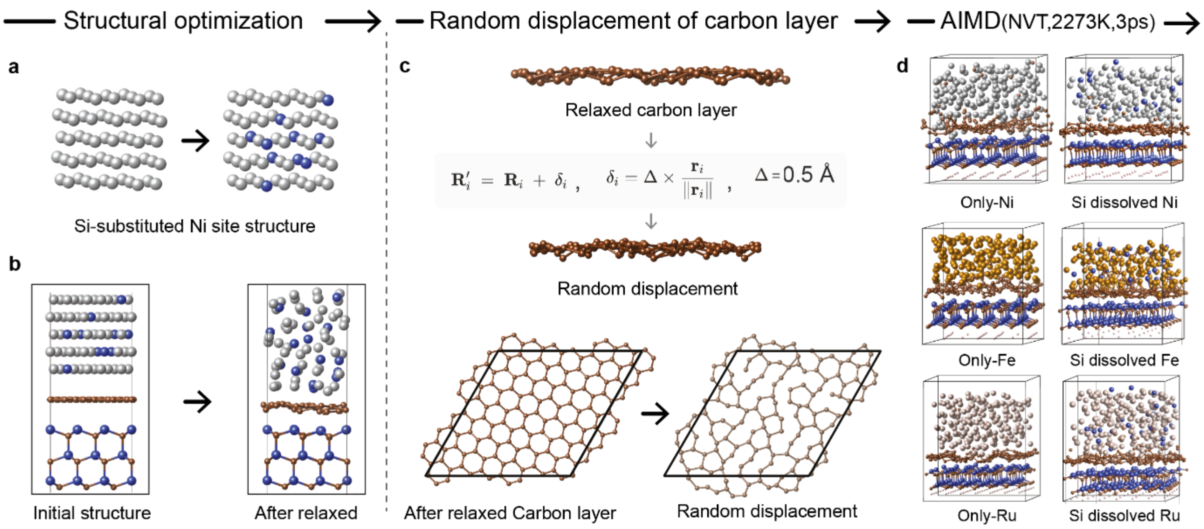

Supplementary Fig. 4 | Modeling workflow and AIMD simulations for the SiC/graphene/metal heterostructures. a, Formation of Si-containing metal layers. **b,** An example of a relaxed configuration of the SiC/Graphene/Metal model after energy minimization. **c,** Generation of randomly-displaced carbon atoms in the graphene layer to study the stabilization effect of metal catalysts. **d,** Model configurations used in this study. Both pure and Si-containing metal layers were investigated for each metal using AIMD simulations.

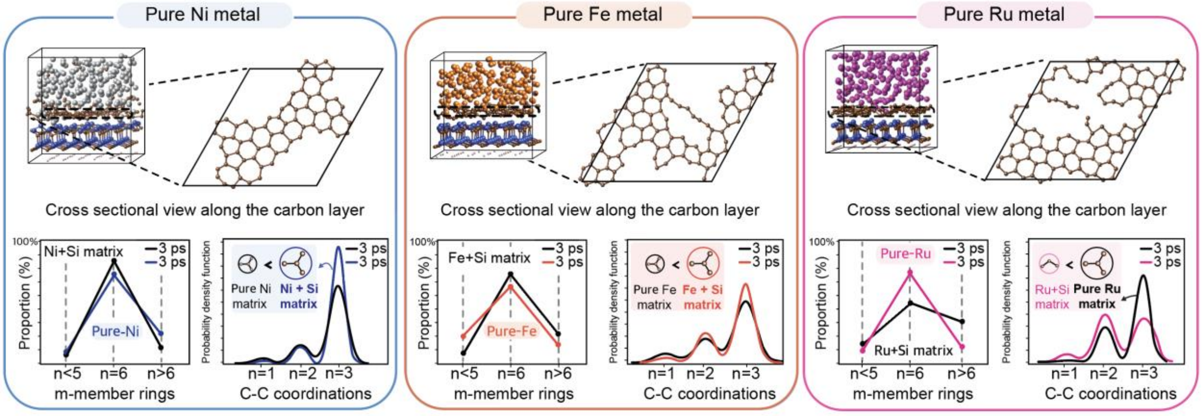

Supplementary Fig. 5 | AIMD simulations with metal layers without Si alloying. For pure Ni and Fe models, the number of six-fold rings and three-fold-coordinated carbon atoms was consistently lower than in their Si-dissolved counterpart, underscoring the critical role of dissolved silicon in enhancing the structural transition toward graphene-like configurations. In contrast, graphene formation in the Ru matrix occurs only when silicon is not dissolved in the Ru bulk. Among the models studied, only the Si-dissolved Ni model provided an environment where carbon atoms could readily reorganize, enabling the formation of stable, two-dimensional graphene configurations.

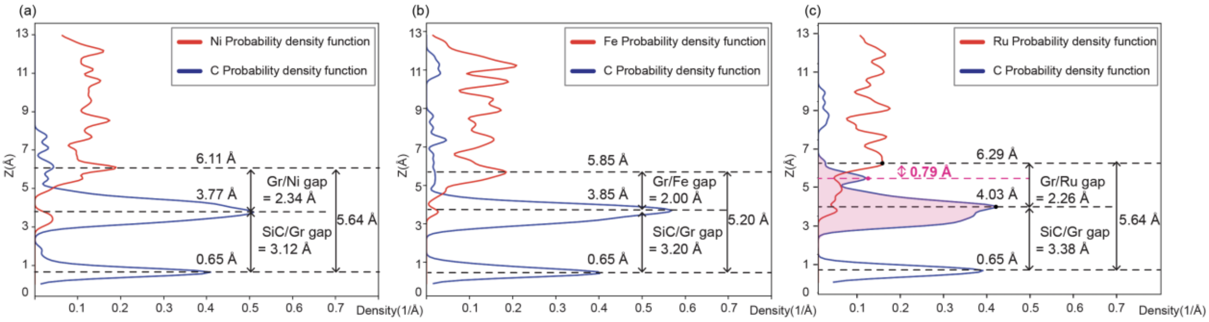

Si containing Ni metal (3ps) Si containing Fe metal (3ps) Si containing Ru metal (3ps)

Supplementary Fig. 6 | Study on the van der Waals gap between the metal and carbon layers using the probability-density function. The width of the van der Waals gap observed in (a) the Si-dissolved Ni model, (b) the Si-dissolved Fe model, and (c) the Si-dissolved Ru model. The Ni-containing model maintained a consistent van der Waals gap between the metal and the topmost carbon layer, whereas the Fe- and Ru-containing models exhibited a collapse of the gap.

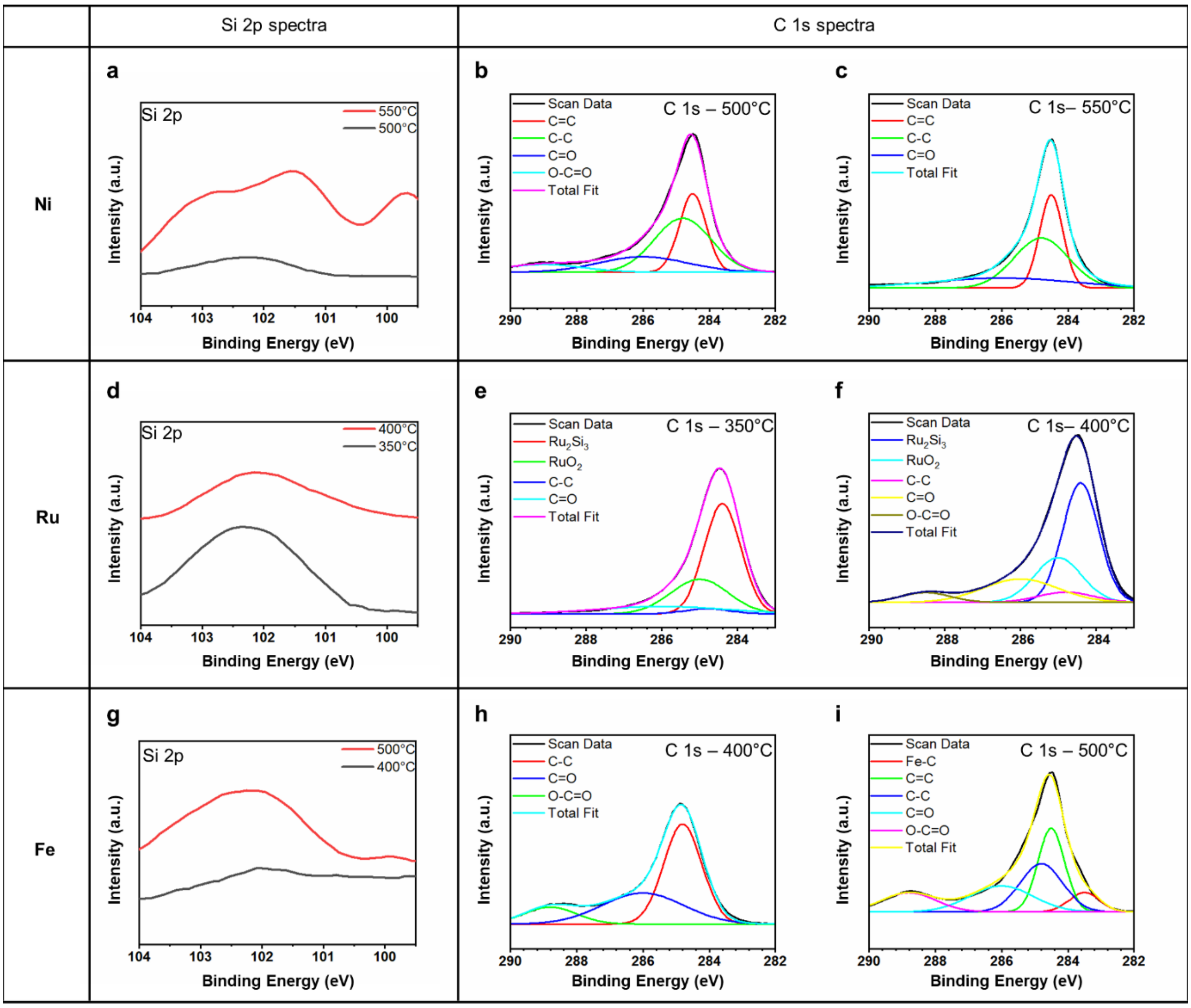

Supplementary Fig. 7 | X-ray photoelectron spectra of metal/SiC after annealing at various temperatures. a, Comparison of the Si 2p spectra in Ni/SiC for each annealing temperature. **b**, C 1s spectra of Ni/SiC annealing at 500ºC. **c,** C 1s spectra of Ni/SiC annealing at 550ºC. **d,** Comparison of the Si 2p spectra in Ru/SiC for each annealing temperature. **e**, C 1s spectra of Ru/SiC annealing at 350ºC. **f,** C 1s spectra of Ru/SiC annealing at 400ºC. **g,** Comparison of the Si 2p spectra in Fe/SiC for each annealing temperature. **h**, C 1s spectra of Fe/SiC annealing at 400ºC. **i,** C 1s spectra of Fe/SiC annealing at 500ºC. All spectra were calibrated using the C-C bond (284.8eV) and cross-checked with Raman spectra (see Supplementary Fig. 8) and XRD (see Supplementary Fig. 9) results. The thickness of the deposited metal layer exceeded the detection limit depth of XPS (typically around 10nm) indicating that the detected Si and C atoms originated from the SiC.

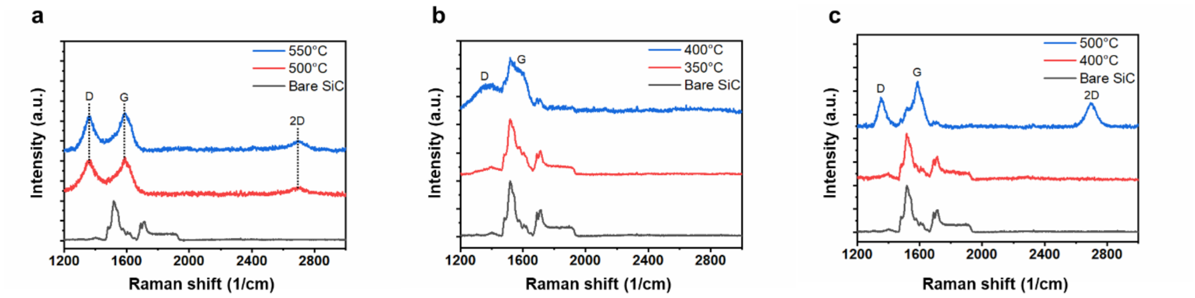

Supplementary Fig. 8 | Raman spectra after annealing at corresponding temperatures. a, Comparison of the Ni/SiC Raman spectra at different annealing temperatures. **b**, Comparison of the Ru/SiC Raman spectra at different annealing temperatures. **c**, Comparison of the Fe/SiC Raman spectra at different annealing temperatures. At 500ºC for Ni, 400ºC for Ru, and 500ºC for Fe, liberated carbon diffused outward and formed graphene on the metal surface, consistent with XPS results.

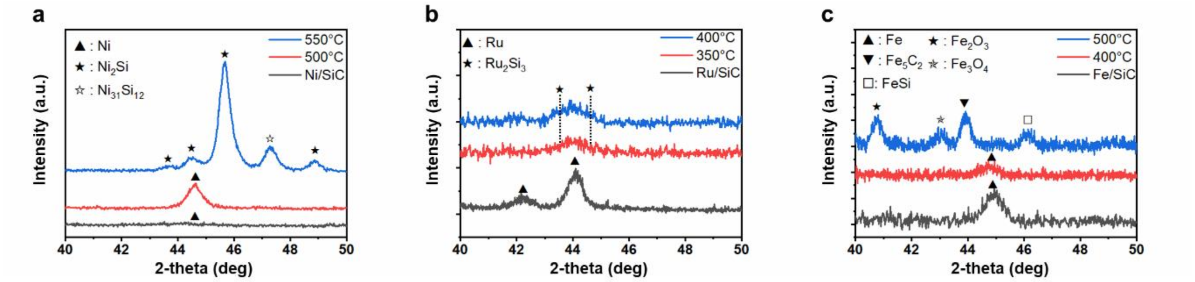

Supplementary Fig. 9 | X-ray diffraction patterns after annealing at corresponding temperatures. a, Comparison of the Ni/SiC X-ray diffraction patterns at various annealing temperatures. The reference patterns correspond to JCPDS no. 71-4655 for Ni, JCPDS no. 79-3559 for Ni_2Si, and JCPDS no. 17-0222 for $Ni_{31}Si_{12}$. **b**, Comparison of the Ru/SiC X-ray diffraction patterns at various annealing temperatures. The reference patterns correspond to JCPDS no. 73-7011 for Ru, and JCPDS no. 88-0895 for Ru_2Si_3. **c**, Comparison of the Fe/SiC X-ray patterns at various annealing temperatures. The reference patterns correspond to JCPDS no. 76-6588 for Fe, JCPDS no. 79-3559 for FeSi, JCPDS no. 89-8103 for Fe2O3, JCPDS no. 71-6336 for Fe_3O_4, and JCPDS no. 89-8968 for Fe_5C_2.

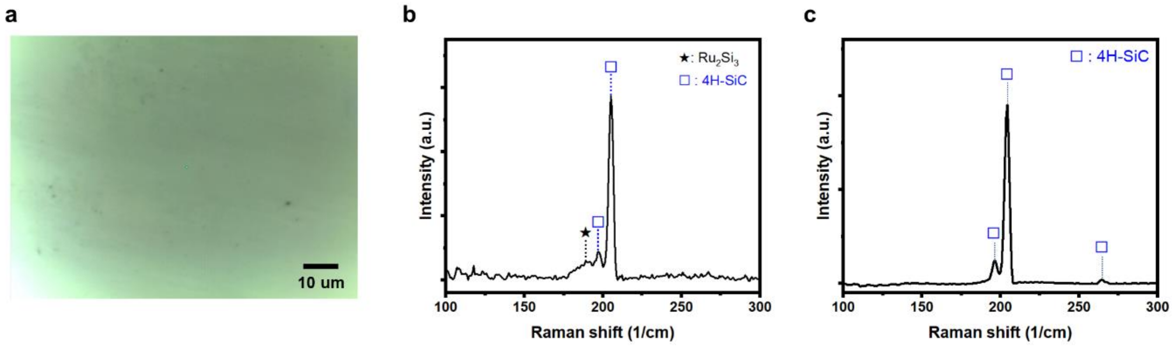

Supplementary Fig. 10 | Optical image and Raman spectra of the Ru/SiC annealed at 350° C. a-b, Raman spectra with optical image reveal the presence of Ru_2Si_3 peak at the 203 cm^{-1}, consistent with XPS and XRD results. **c,** Raman spectra of bare SiC in range of 50 cm^{-1} to 500 cm^{-1}, indicate the absence of the 203 cm^{-1} peak.

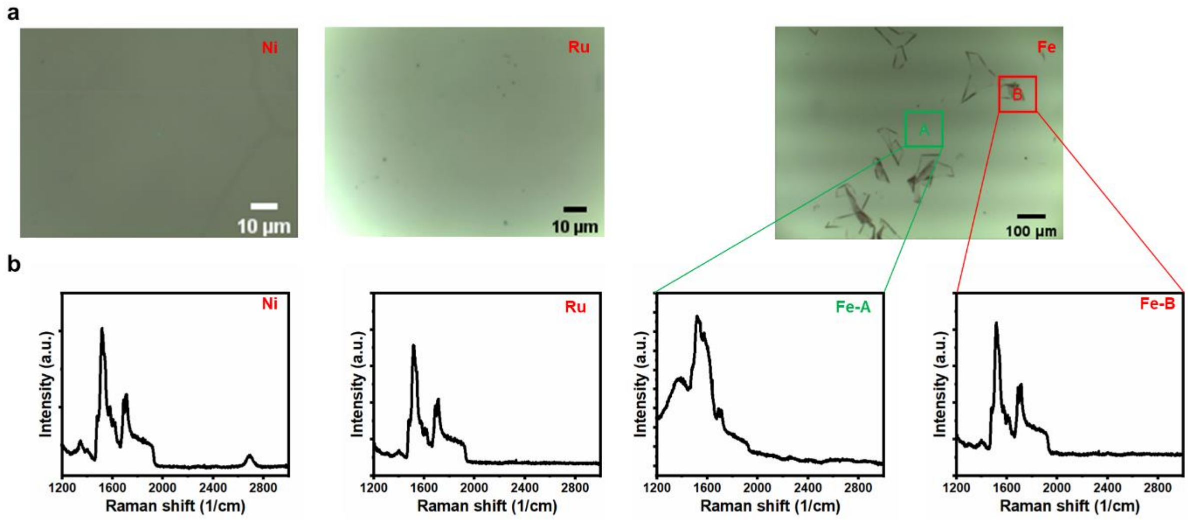

Supplementary Fig. 11 | Micrography and Raman spectra of various metals on SiC after annealing at corresponding temperatures and etching with the appropriate etchant. a, Micrography of Ni/SiC annealed at 500°C and etched with $FeCl_3$, Fe/SiC annealed at 400°C and etched with $FeCl_3$, and Ru/SiC annealed at 350°C and etched with NaOCl. **b,** Raman spectra of each result, showing that only Ni enables the graphene formation on SiC.

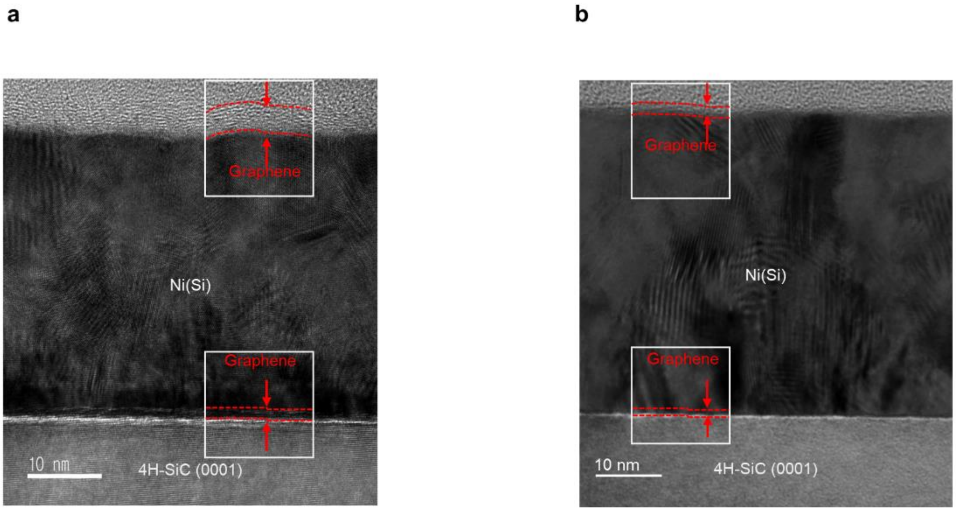

Supplementary Fig. 12 | TEM images of Ni/SiC structure annealed at 500°C and 320°C respectively, measured at 10 nm scale. a, TEM images of Ni/SiC annealed at 500°C. **b,** TEM images of Ni/SiC annealed at 320°C. The TEM images show the graphene layer not only on the metal surface, but also at the Ni/SiC interface. The thickness of graphene is slightly bigger when increasing the annealing temperature, indicating the MAG process is a temperature-driven.

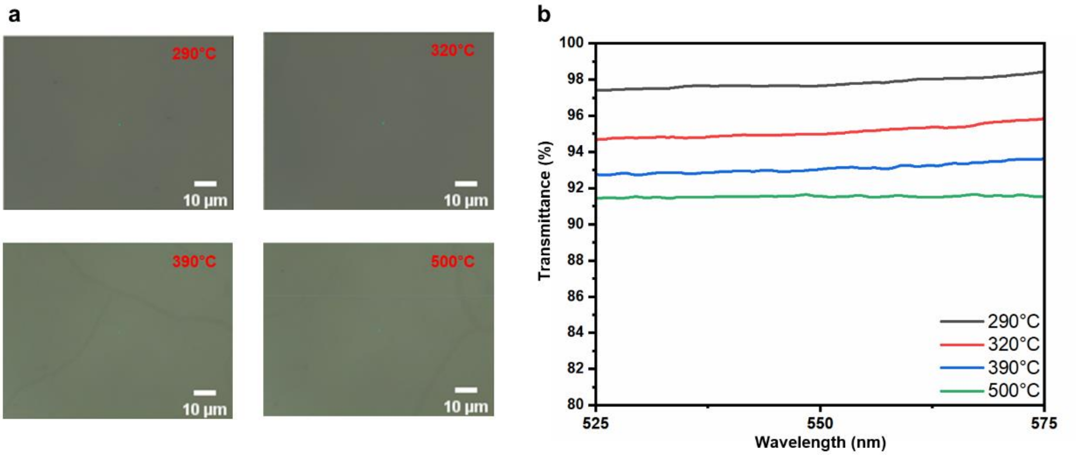

Supplementary Fig. 13 | Optical images and UV-visible spectra after annealing at the corresponding temperatures and etching with $FeCl_3$. a, Optical images after annealing at corresponding temperatures and etching, confirming the absence of residuals and the formation of a macroscopic graphene film. **b,** UV-visible spectra showing that the MAG process is driven by temperature.

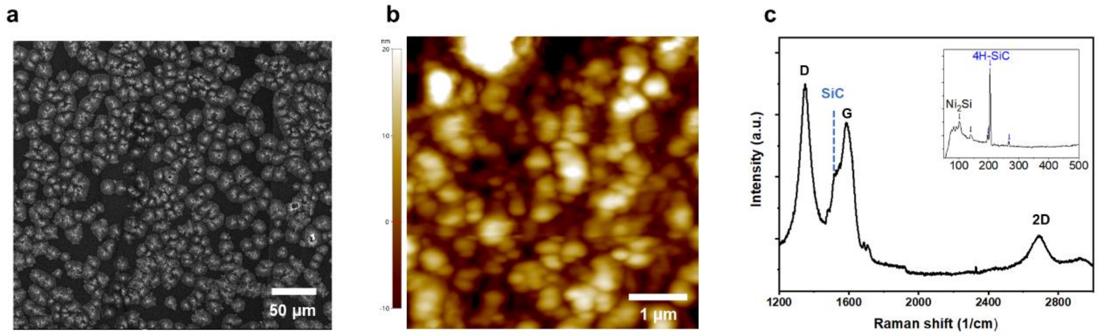

Supplementary Fig. 14 | SEM, AFM images, and Raman spectra after annealing above the silicide formation temperature, and etching the Ni layer with $FeCl_3$. a-b, SEM, and AFM images reveal inhomogeneous reactions, confirming the formation of a non-uniform clustered film. **c,** Raman spectra indicate that the clustered films comprise graphene on a silicide layer.

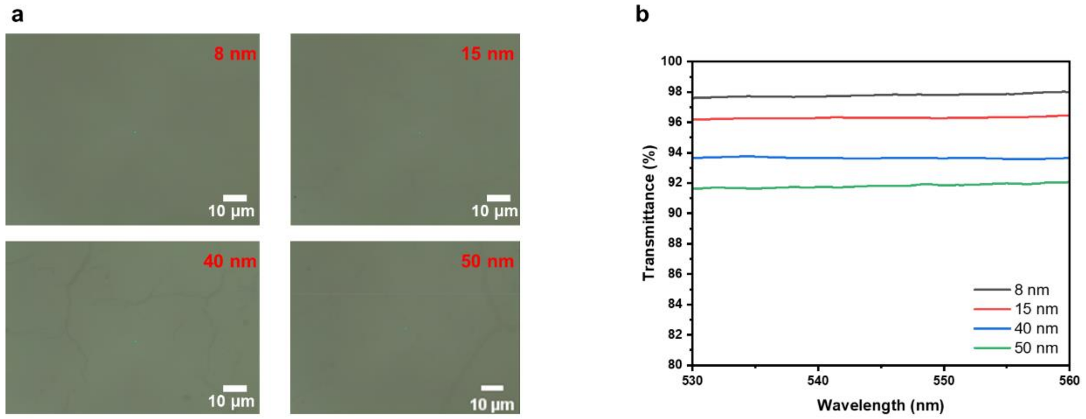

Supplementary Fig. 15 | Optical images and UV-visible spectra for various metal thickness used in MAG process. a, Optical images of samples with different metal thicknesses. **b,** UV-visible spectra indicating that graphene thickness decreases with reduced metal thickness.

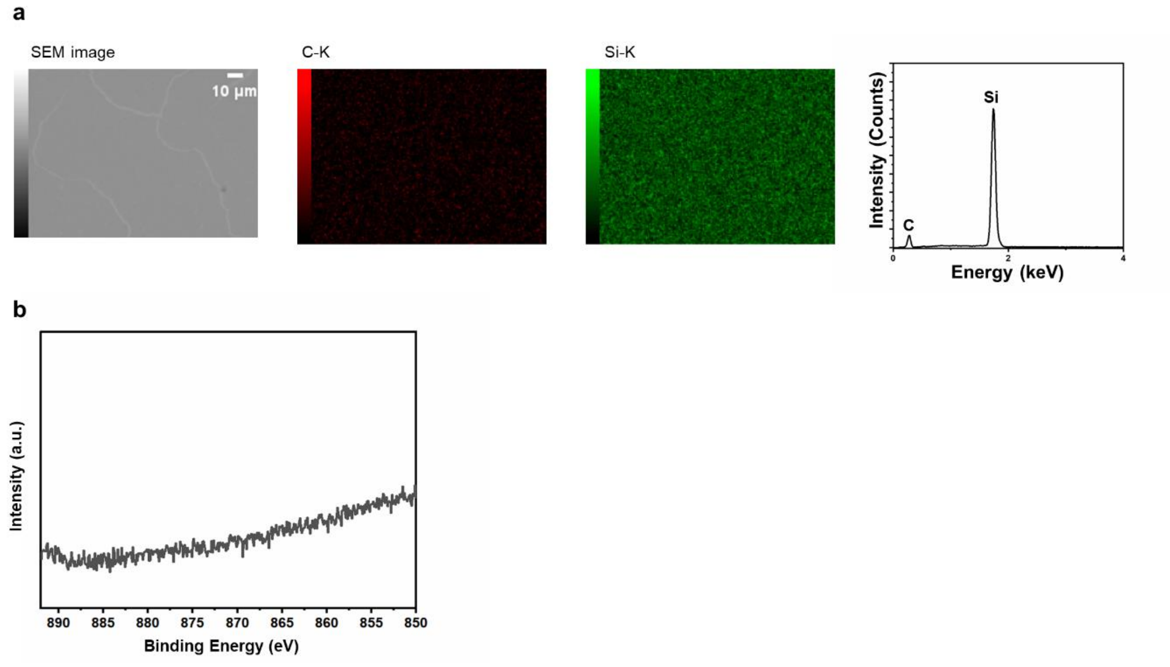

Supplementary Fig. 16 | Energy-dispersive X-ray (EDS) spectra and Ni 2p XPS after etching the unreacted Ni layer with $FeCl_3$. a, EDS scan shows no Ni atoms remaining on the surface. **b,** XPS Ni 2p spectra confirm the absence of detectable Ni. All results indicate the complete removal of Ni.

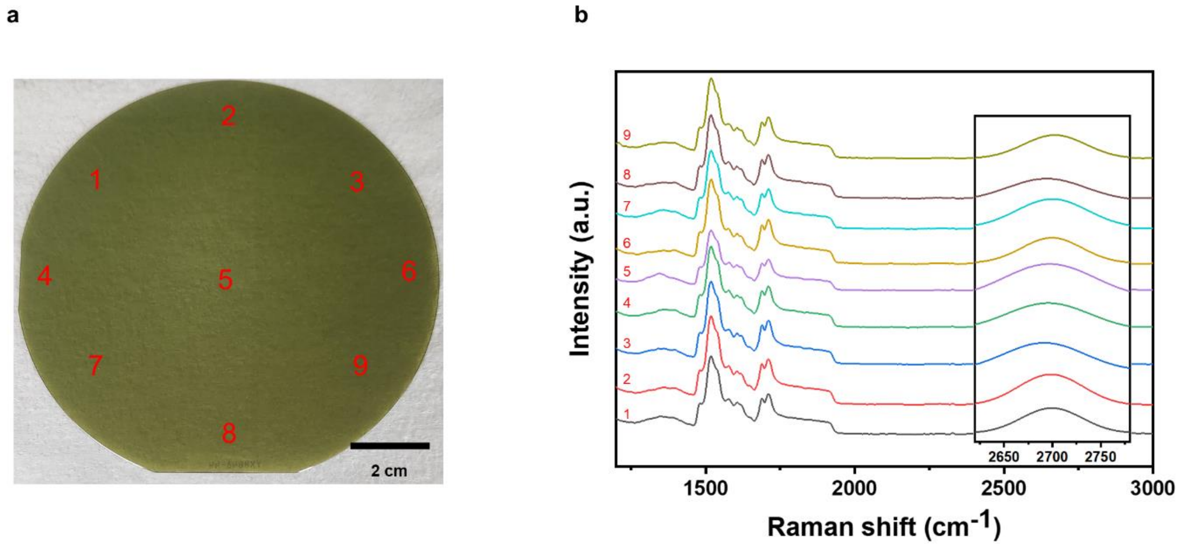

Supplementary Fig. 17 | Raman spectra of a graphitized 4-inch wafer. The wafer was divided into nine areas, and Raman spectra from all regions consistently show the characteristics D, G, and 2D peaks of graphene.

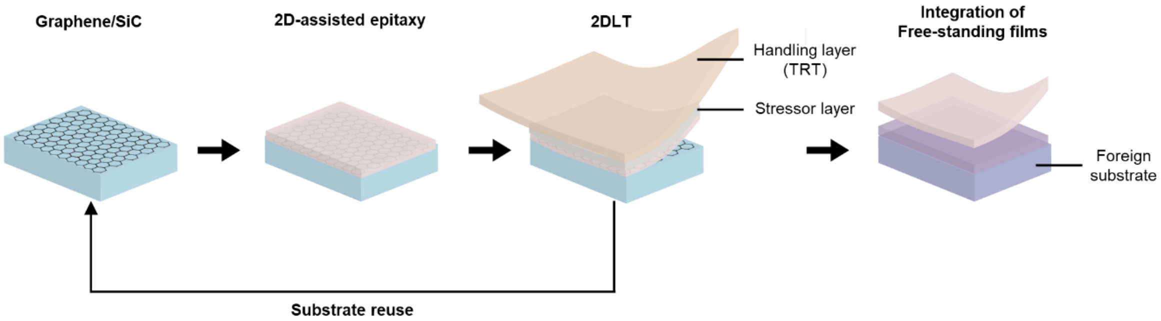

Supplementary Fig. 18 | Schematic illustration of 2D-assisted epitaxy process. The process begins with the graphitization of the SiC to synthesize graphene. This graphitized template is then prepared for 2D-assisted epitaxy, where a wide-bandgap material is grown using a growth chamber, such as MOCVD or MBE, under optimized conditions. After the growth, a stressor layer, typically Ni, is deposited via a sputtering or E-beam evaporator. The thickness and deposition conditions of the Ni layer must be carefully controlled to enable precise exfoliation of the membrane at the van der Waals gap between the membrane and the graphitized SiC interface. Additionally, an adhesion layer may be employed to prevent peeling of the stressor layer. A TRT is then applied as a handling layer, and exfoliation is carried out by smoothly lifting the handling layer. The exfoliated freestanding membrane is subsequently transferred to a foreign substrate. Finally, the TRT is removed by heating the membrane-attached-foreign-sample above 110ºC.

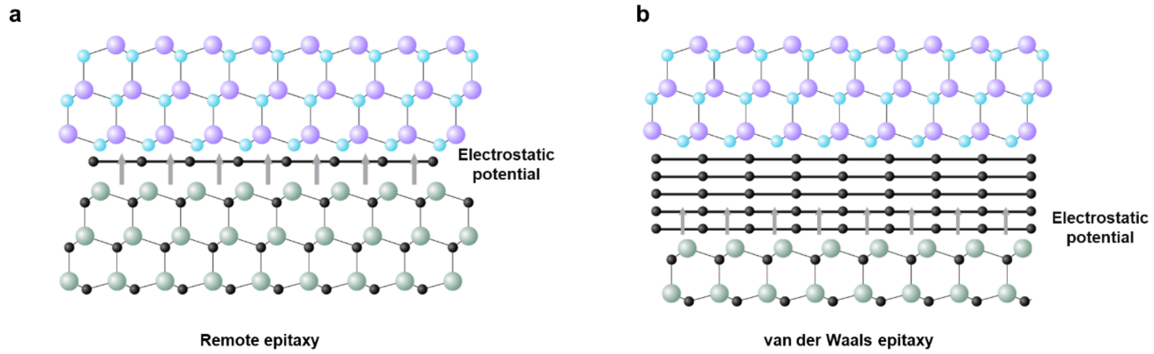

Supplementary Fig. 19 | Schematic illustration of 2D-assisted epitaxy mechanisms. 2D-assisted epitaxy encompasses techniques like remote epitaxy and vdWE, which enable high-quality material growth on 2D materials. However, these techniques differ significantly in their requirements for preparing the graphitized sample. Remote epitaxy requires a minimum graphene layer that is robust enough to withstand the harsh growth environment while allowing the lattice information of the underlying substrate to guide the growth of the crystalline film. In contrast, vdWE does not rely on the lattice information of the substrate. Instead, it demands multi-layers of graphene to completely screen the substrate's electrostatic potential, which enhances the quality of the grown membrane by eliminating substrate interference.

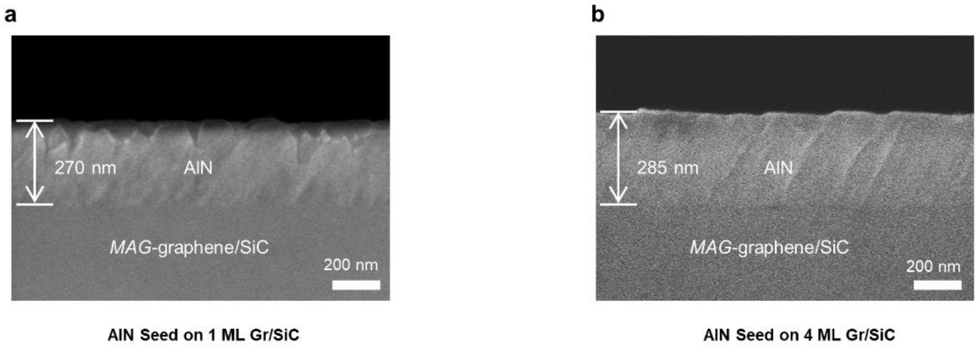

Supplementary Fig. 20 | SEM cross-sectional images of AlN grown on MAG-treated 1 ML graphene and 4 ML graphene on SiC. The thickness of AlN increased from 270 nm to 285 nm, indicating enhanced three-dimensional growth in the vertical direction for the 4 ML graphene sample compared to the 1 ML graphene sample.

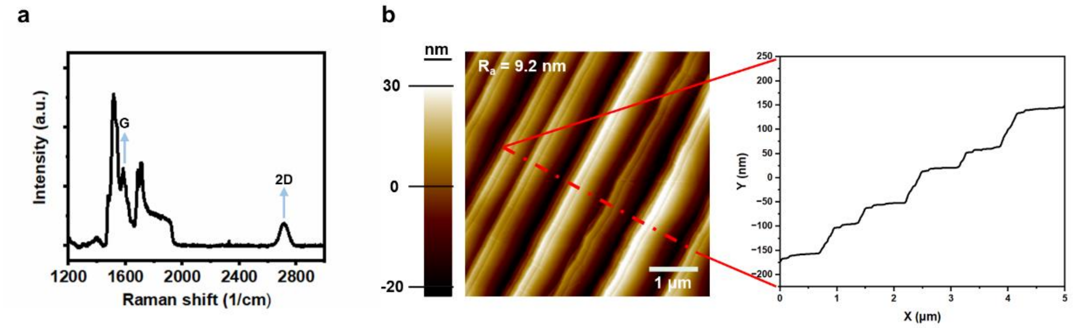

Supplementary Fig. 21 | Raman spectra and AFM images of high-temperature graphitized SiC. a, Raman spectra showing the G and 2D peaks, indicating that graphene covers the entire SiC substrate. **b,** AFM images and line profiles along the red line revealing micrometer-scale terrace widths and nanometer-scale step heights.

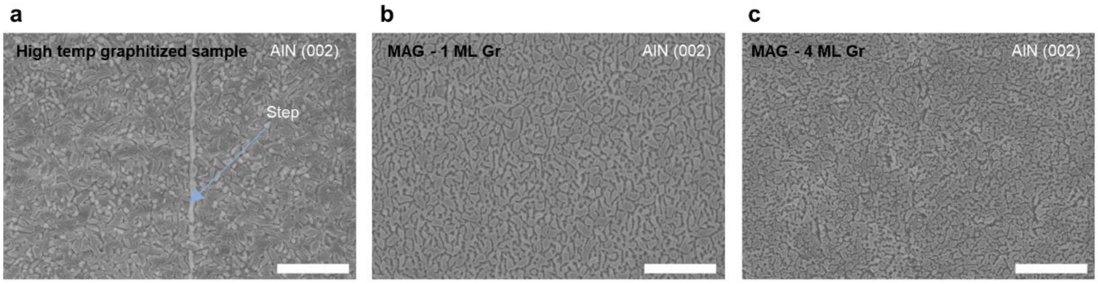

Supplementary Fig. 22 | SEM images of AlN grown on high-temperature graphitized SiC and MAG-graphitized SiC. a, SEM images showing AlN adatoms predominantly nucleating at step edges, with AlN grown on wide terraces exhibiting a poly-crystalline nature. **b-c**, SEM images demonstrating unidirectional growth of AlN crystallites, indicating a single-crystalline nature on both 1 ML Gr/SiC and 4 ML Gr/SiC templates. The scale bar in the SEM images is 300 nm.

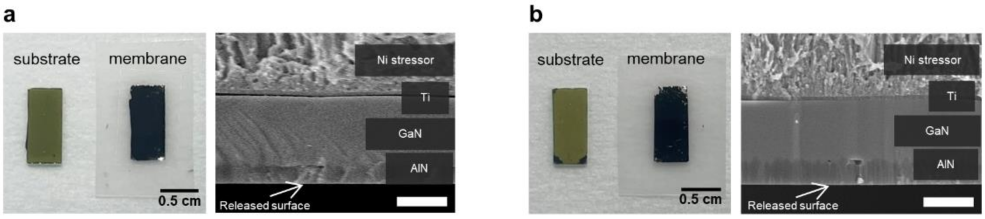

Supplementary Fig. 23 | Camera and SEM images of GaN/AlN grown on MAG-graphitized SiC templates. a, Camera and SEM images of exfoliated GaN/AlN grown on 1 ML Gr/SiC. **b,** Camera and SEM images of exfoliated 4 ML Gr/SiC. Both camera images demonstrate the successful exfoliation of the grown films from the MAG-graphitized SiC templates. The SEM images reveal macroscopically smooth surfaces of the exfoliated films, confirming the effectiveness of the 2DLT process. The scale bar in the SEM images is 500 nm.

Supplementary Table. 1 | Comparison of the crystalline quality of GaN/AlN on MAG-treated SiC with GaN grown on other substrates. The results suggest that our MAG-treated SiC offers a desirable platform for GaN materials. LT refers to low-temperature growth.

Material	**Buffer layer**	**Substrate**	**Growth Method**	**(002) FWHM (arcsec)**	**Reference**
GaN	LT-GaN	Al_2O_3	MOCVD	220	[5]
	LT-AlN	Al_2O_3		380	[5]
	AlN/h-BN	Al_2O_3		576	[6]
	-	SiC		423	[7]
	AlN	SiC		200	[8]
	Graphene	SiC		222	[9]
	AlN/Graphene	SiC		1260	[10]
	AlN/Graphene	*SiC*		*385*	*This work*

Supplementary References

1. Dardzinski, D., Yu, M., Moayedpour, S. & Marom, N. Best practices for first-principles simulations of epitaxial inorganic interfaces. *Journal of Physics Condensed Matter* vol. 34 Preprint at https://doi.org/10.1088/1361-648X/ac577b (2022).

2. Nash, B. P. & Nash, A. The Ni-Si (Nickel-Silicon) System Equilibrium Diagram. *Bulletin of Alloy Phase Diagrams* **8**, 6–14 (1987).

3. Vojt~crtovsk', K. & Zem~ik, T. MOSSBAUER STUDY OF THE Fe-Si INTERMETALLIC COMPOUNDS. *Czechoslovak Journal of Physics B* **24**, 171–78 (1974).

4. Perring, L., Bussy, F., Gachon, J. C. & Feschotte, P. *The Ruthenium-Silicon System*. *Journal of Alloys and Compounds* vol. 284 (1999).

5. Bayram, C., Pau, J. L., McClintock, R. & Razeghi, M. Delta-doping optimization for high quality p -type GaN. *J Appl Phys* **104**, (2008).

6. Kobayashi, Y., Kumakura, K., Akasaka, T. & Makimoto, T. Layered boron nitride as a release layer for mechanical transfer of GaN-based devices. *Nature* **484**, 223–227 (2012).

7. Xie, Z. Y. *et al.* Effects of surface preparation on epitaxial GaN on 6H-SiC deposited via MOCVD. in *MRS Internet Journal of Nitride Semiconductor Research* vol. 4 (Materials Research Society, 1999).

8. Reitmeier, Z. J. *et al.* Surface and defect microstructure of GaN and AlN layers grown on hydrogen-etched 6H-SiC(0001) substrates. *Acta Mater* **58**, 2165–2175 (2010).

9. Kim, J. *et al.* Principle of direct van der Waals epitaxy of single-crystalline films on epitaxial graphene. *Nat Commun* **5**, (2014).

10. Yu, Y. *et al.* Demonstration of epitaxial growth of strain-relaxed GaN films on graphene/SiC substrates for long wavelength light-emitting diodes. *Light Sci Appl* **10**, (2021).

Other Supplementary Materials for this manuscript include:

Supplementary Video 1. AIMD simulation of the Ni/graphitic carbon/SiC system.

Supplementary Video 2. AIMD simulation of the Fe/graphitic carbon/SiC system.

Supplementary Video 3. AIMD simulation of the Ru/graphitic carbon/SiC system.